Received: 15 October 2021 | Revised: 26 February 2022 | Accepted: 22 May 2022

IET Power Electronics

DOI: 10.1049/pel2.12337

The Institution of Engineering and Technology WILEY

ORIGINAL RESEARCH

Integrated current balancing cells based IPOP bidirectional CLLC resonant converter modules for high-power applications

Ubaid Ahmad[1] | **Honnyong Cha**[1] | **Jong-Suk Ro**[2]

[1]Department of Environmental and Energy Engineering, Kyungpook National University, Daegu, South Korea

[2]School of Electrical and Electronics Engineering, Chung-Ang University, Dongjak-gu, Seoul, 06974, Republic of Korea

Correspondence
Ubaid Ahmad, Department of Environmental and Energy Engineering, Kyungpook National University, Daegu, South Korea.
Email: ubaidahmad@knu.ac.kr

Jong-Suk Ro is with School of Electrical and Electronics Engineering, Chung-Ang University, Building 310, Room 633, Dongjak-gu, Seoul, 06974, Republic of Korea
Email: jongsukro@gmail.com

Funding information
National Research Foundation of Korea (NRF); Ministry of Science and ICT, Grant/Award Number: NRF-2022R1A2C2004874

Abstract

This paper proposes an integrated current balancing (ICB) cells-based input parallel output parallel (IPOP) bidirectional CLLC modules. The IPOP system based on the CLLC modules inherent all of the good features of a single CLLC module including zero-voltage and zero-current switching (ZVZCS) for the inverter and rectifier stage. Besides, the IPOP configuration is a better approach to utilize low-power rating modules for high-power applications. However, tolerances in the tank circuit parameters cause an acute imbalance in modules currents. Therefore, the equal power distribution among the IPOP CLLC modules is an important issue that needs to be addressed. Different control and passive current sharing techniques have been proposed, but they cause increase in component count, cost, complexity, and magnetic volume of the IPOP converters. This paper integrates the already present resonant inductors of the bidirectional CLLC modules to evenly share the two currents at the input as well as at the output of the converters under the open-loop condition with substantial tolerances of ± 10 % in the tank circuit parameters. Moreover, the proposed ICB cells generate sufficient resonant inductances for the respective tank circuits, simultaneously. No additional active or passive components are introduced in the system; thus, it does not increase the cost, complexity, and magnetic volume of the IPOP CLLC modules. Two types of cores (UU- and EE-cores) based ICB cells are analysed with current sharing performance. To verify the effectiveness of the ICB cells, a 4.9-kW laboratory hardware prototype was built and tested.

1 | INTRODUCTION

With increased power ratings of the converters, the numbers of paralleled power stages in a single power converter or the IPOP converters configuration with individual low-power converters keep increasing. However, the current sharing between the IPOP converters is highly demanding because of the uneven current distribution in the system, which may cause uneven thermal stresses, degrade converter performance, reduce system reliability, and even causes modules failure in the IPOP system [1]. In adverse, with promising current sharing techniques, the IPOP system offers certain advantages such as; better thermal distribution, high-frequency operation, high-power density, relatively easy design, and fabrication of low-power rating modules when compared to high-power rating modules, and selection of switching devices with reduced current stress makes it more attractive for practical use [1].

As discussed, that the IPOP system has several advantages; however, tolerances in the resonant tank circuit parameters make the IPOP system unreliable. An acute imbalance in constituent modules currents can be observed, which leads to run away condition in the IPOP converters [2]. Recently, plethora of research has been carried out to address the power imbalance issue in the IPOP converters. These current sharing (CS) techniques includes; control based CS [2–9], structural based CS [10, 11], and passive current sharing including; magnetic [12–16], and capacitive CS technique [17, 18]. These CS techniques can relieve or eliminate the effect of uneven power distribution in the IPOP converters, as depicted in Figure 1. A comprehensive review and comparison of different control schemes for

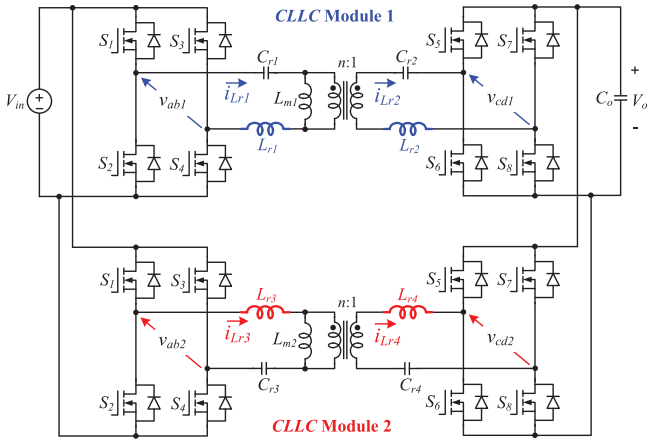

FIGURE 1 IPOP system configuration based on bidirectional CLLC modules

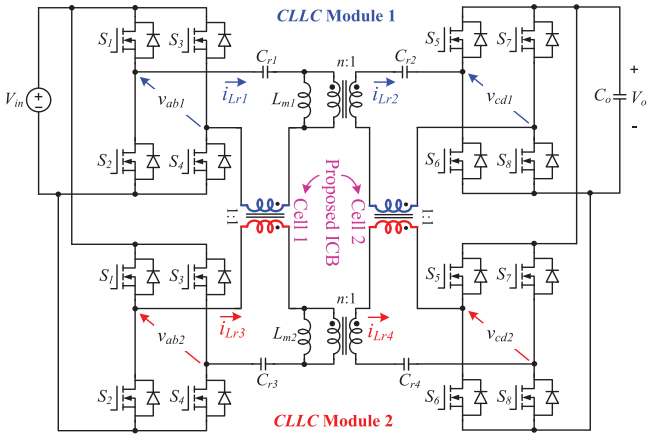

FIGURE 2 Proposed ICB cells based IPOP two bidirectional CLLC modules

parallel converters are given in [3]; including droop control scheme [4], and master-slave scheme [5]. However, complicated control schemes are more vulnerable to failure, which reduces system reliability. Moreover, feedback control components increase the cost of the system.

In addition, the others control schemes that relieve the effect of uneven CS in resonant converters are addressed in [6–9]. In [6] proposes the IPOP LLC modules; however, the CS performances with mismatched parameters are not addressed. A CS method for the IPOP LLC modules with partial energy processing is presented in [7]; where, a transformer and auxiliary DC–DC converter are introduced for even CS in each phase and CS is realized by controlling the duty cycle of the auxiliary converter. However, additional transformer with DC–DC converter and complex control loops are required with each phase, which increases the cost and complexity of the IPOP converters. In [8], the output voltage of the power factor correction (PFC) stage is varied to compensate for the power imbalance caused by the tolerances in tank circuit parameters. However, a PFC stage is required to evenly share the currents among the IPOP LLC modules. In [9], variable and fixed value inductors are added to the IPOP two LLC modules. The variable inductor is responsible to compensate gain characteristic tolerances and realizes even current sharing in the IPOP two LLC modules.

The input series output parallel (ISOP) and input parallel output series (IPOS) type configuration are presented in [10, 11]. The currents are forced to be the same due to series connection on either on primary or at the secondary side of the transformers. However, the current stress on the primary side in ISOP and on the secondary side in IPOS cannot be alleviated, which is equal to the conventional single LLC converter.

Besides, in case of passive CS strategies, the magnetic-based strategies are addressed in [12–16]. In [12], a spatial magnetic core with a current balancing transformer has been utilized for a three-phase LLC converter. However, it utilizes a customized spatial core, which increases the cost and complexity. Besides, strategy in [12] is suitable for three-phase topology and applied to unidirectional power flow applications. The magnetic coupling current balancing (MC-CB) cell based IPOP LLC modules are presented in [13]. It can achieve the current sharing in the open-loop condition; however, this method utilizes additional inductors with the MC-CB cells to ensure even current sharing among the IPOP LLC modules. Therefore, it increases the magnetic volume, cost, and decreases the power density of the IPOP converters. Both [13–15] CS strategy is applied to unidirectional LLC converters. Besides, [13–15] does not explain the CS on the secondary side of the IPOP converters with mismatches in the main transformers parameters. Moreover, the CS using single magnetic link is also not reported in [13–15]. For bidirectional power flow, the CS in IPOP dual active bridge (DAB) converters based on magnetic strategy is presented in [16]. However, additional magnetics are introduced for even current sharing with power transferring series inductors, which increases magnetic volume, and cost of the IPOP DAB converters. Furthermore, the charge balance condition of capacitors-based CS is reported in [17, 18]. In [17], an additional flying capacitor is employed to realize even CS in two-phase LLC converter. Similarly, two flying capacitors are added in the circuit to realize CS in asymmetric three-phase LLC converter in [18]. The idea in [18] is the extension of [17]. However, the topology extension for more than three or four phases is not recommended due to the design difficulties of asymmetric resonance operation. Besides, they increase the cost of the IPOP converters with additional capacitors. The current sharing strategies from [12, 16–18] also does not explain the even current distribution at the secondary side of the converter with mismatches in the main transformers parameters.

Previous research on current balancing extensively cover the LLC converter based IPOP system [7–15], and [17, 18]; however, the current sharing in the IPOP system based on bidirectional CLLC modules are not given as much attention. This paper proposed ICB cells based IPOP bidirectional CLLC modules, as shown in Figure 2. The proposed method integrates the already present inductors to ensure even current sharing

with significant tolerances in the circuit parameters as well as complete the resonance operation for constituent CLLC modules. Hence, it does not require additional hardware or magnetic components, and expensive sensors. As a result, it does not increase the cost, complexity, and magnetic volume of the IPOP CLLC modules. Besides, this paper deals with the mismatches in the main transformers as well. In addition, it can ensure CS using single magnetic link in IPOP two CLLC modules. Moreover, two types of cores structures (UU- and EE-cores) for the ICB cells are introduced and analysed in detail. The EE-cores based ICB cell requires two while UU-cores ICB cells require four cores to shape a single ICB cell. Thus, it can reduce the number of cores with EE-cores structure.

2 | CURRENT SHARING PERFORMANCE OF THE IPOP TWO BIDIRECTIONAL CLLC MODULES

The resonant converters offer a number of advantages including; soft-switching in all switches, low EMI concern, eliminate the need for clamp or snubber circuit, high-frequency operation, high-power density, and high efficiency. Among the resonant converters, the LLC converter is the most popular topology for wide input and output voltage applications [20, 21]. However, it is only suitable for unidirectional power transfer. In case of the bidirectional power flow, a bidirectional LLC resonant converter is presented in [22, 23]. It can achieve soft switching in the whole load range as well as bidirectional operation. However, in reverse power flow direction, the switching bridge voltage directly appears across the magnetizing inductance, and it is no longer part of the tank circuit, which changes the LLC tank circuit properties into a series resonant converter (SRC). The SRC faces a light-load regulation problem, and the operating frequency should increase considerably as the input voltage increase, which makes the SRC inappropriate for wide input and output voltage applications. A bidirectional CLLC resonant converter is presented in [24, 25]. This topology is suitable for soft-switching operation with bidirectional power flow without any additional snubber circuitry. Besides, voltage stresses of primary and secondary switches are confined to input and output voltages.

2.1 | Current sharing performance of the IPOP two bidirectional CLLC modules

The IPOP system based on bidirectional CLLC resonant converters illustrated in Figure 1 have the full-bridge symmetric structure of the primary inverting stage and secondary rectifying stage with high-frequency isolation transformers. These transformers are designed with magnetizing inductances L_{m1}, L_{m2} and turns ratio of 1:1. Whereas $L_{r1/3}$, $L_{r2/4}$, $C_{r1/3}$ and $C_{r2/4}$ are the series inductors and capacitors of symmetric tank circuits of CLLC module 1 and 2, respectively.

TABLE 1 Tank circuit parameters with defined mismatches of the IPOP two bidirectional CLLC modules

	Resonant inductor (L_r)	Resonant capacitor (C_r)	Magnetizing inductance (L_m)
Module 1 (Reference)	$L_{r1} = 36.5\ \mu H$	$C_{r1} = 222\ nF$	$L_{m1} = 167\ \mu H$
Case 1:	$L_{r3} = 1.1L_{r1}$	$C_{r3} = 1.1C_{r1}$	$L_{m2} = 1.1L_{m1}$
Module 2	$L_{r4} = 1.1L_{r2}$	$C_{r4} = 1.1C_{r2}$	
Case 2:	$L_{r3} = 0.9L_{r1}$	$C_{r3} = 1.1C_{r1}$	$L_{m2} = 1.1L_{m1}$
Module 2	$L_{r4} = 0.9L_{r2}$	$C_{r4} = 1.1C_{r2}$	
Case 3:	$L_{r3} = 1.1L_{r1}$	$C_{r3} = 0.9C_{r1}$	$L_{m2} = 1.1L_{m1}$
Module 2	$L_{r4} = 1.1L_{r2}$	$C_{r4} = 0.9C_{r2}$	
Case 4:	$L_{r3} = 1.1L_{r1}$	$C_{r3} = 1.1C_{r1}$	$L_{m2} = 0.9L_{m1}$
Module 2	$L_{r4} = 1.1L_{r2}$	$C_{r4} = 1.1C_{r2}$	

There are multiple possible cases of tolerances in the IPOP system; however, tolerances in the resonant tank circuit parameters are more practical and may cause an acute imbalance in the input as well as in the output currents. Therefore, this paper explains the current sharing in the IPOP two CLLC modules with intentional ±10 % tolerances in circuit parameters. These tolerances are quantified and listed in Table 1. Such as; $L_{r3} = a \times L_{r1}, L_{r4} = b \times L_{r2}, C_{r3} = c \times C_{r1}, C_{r4} = d \times C_{r2}$, and $L_{m2} = e \times L_{m1}$, where a, b, c, d, and e are the defined tolerances of constituent CLLC modules. Theoretically, tolerances in three parameters can lead to a total of eight ($2^3 = 8$) possible combinations of mismatched conditions. However, the last four cases are the replica of the first four ones in case of current sharing error in the IPOP system. The only difference is in the current distribution between the constituent CLLC modules. Whenever, the difference between the resonance frequencies and switching frequency of the constituent CLLC modules increase the current sharing become worsen in it. Moreover, the higher gain of tank circuits in constituent CLLC modules will deliver more power as compared to the lower gain tank circuits. It can be analysed using the k–Q gain curves of the CLLC module [24]. The parameters of module 2 in cases 1 and 4 deviates in the same direction, thus, the difference between the resonance frequencies in cases 1 and 4 are high compared to the other two cases. These two cases are the possible worst-cases with only difference in magnetizing inductances. Therefore, case 1 with a higher magnetizing inductance is considered for experimental verification in Section 5, which has lower conduction and switching losses as compared to case 4 [24].

The current sharing performance is evaluated through simulation results in PSIM, as shown in Figure 3. Figure 3a,b are the simulation results of modules 1 and 2 using case 1 parameters for module 2. It can be seen from the waveforms that the whole power is delivered by module 1 while module 2 does not take part in transferring power to the load. As a result, a huge imbalance in currents is observed. Besides, the result of case 1 is the same as that of case 4. In case of cases 2 and 3 as shown in Figures 3c,d, and 3e,f, respectively; the difference in

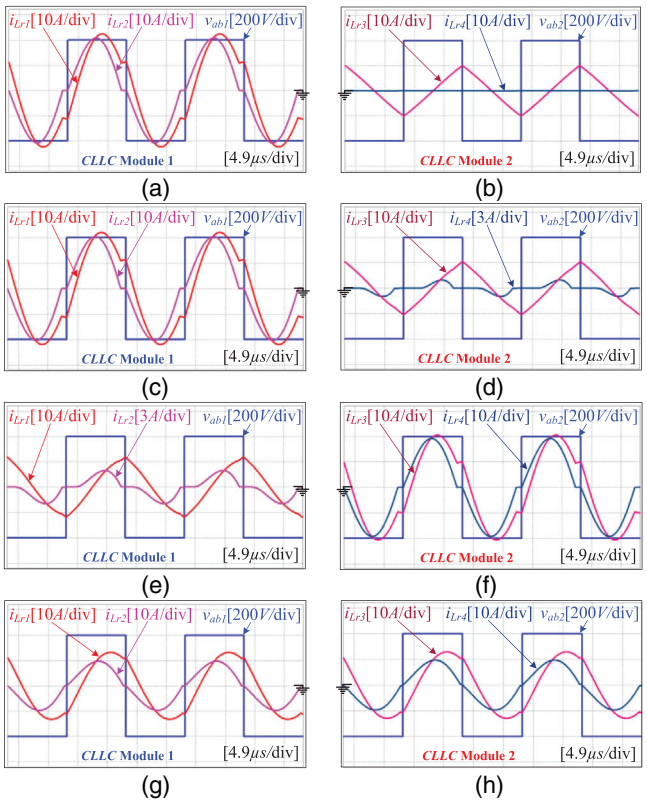

FIGURE 3 Simulation results of the IPOP two bidirectional CLLC modules with mismatched parameters, without and with proposed ICB cells. Where v_{ab1}, v_{ab2} are the primary MOSFETs bridges voltages, and i_{Lr1}, i_{Lr3}, and i_{Lr2}, i_{Lr4} are the primary and secondary side currents of the IPOP two CLLC modules, respectively. (a), (b) Case 1. (c), (d) Case 2. (e), (f) Case 3 results without proposed ICB cells, respectively. (g), (h) Case 1 results with proposed ICB cells

resonance frequencies is small that is why a very small amount of power is delivered by the second module in the IPOP two CLLC modules. In case 2, module 2 takes part in transferring a small amount of power while in case 3 module 1 delivers small amount of power. With higher L_r, the gain of case 3 will be a little high that is why the amount of power delivered by module 1 in Figure 3e is a bit higher than case 2 of module 2 in Figure 3d. Moreover, the current distribution in both cases is decided by the gain of the CLLC modules. In case 2, the gain of module 1 is higher than the gain of module 2. Similarly, in case 3 the gain of module 2 is higher than the gain of module 1. Therefore, the current distribution is opposite in both cases. However, the current sharing is not that severe as in cases 1 and 4, but still an issue needs to be addressed. Simulation results with the proposed ICB cells are shown in Figure 3g,h, which verifies even current sharing in severe imbalance case (case 1) quite effectively in the open-loop condition. Therefore, the proposed method does not require additional magnetics or complicated control schemes to evenly share the input as well as the output currents. It is noteworthy to mention that the principle of current imbalances explained above can be applied to any resonant tank circuit connected in the IPOP configuration.

3 | INTEGRATED CURRENT BALANCING CELLS BASED IPOP TWO BIDIRECTIONAL CLLC MODULES

The proposed ICB cells are the result of the magnetic integration of already present resonant inductors between the constituent CLLC modules. Two inductors of the primary and two of the secondary sides tank circuits shape two ICB cells, which are connected between the leading and lagging leg midpoints at the primary and secondary active bridges of the IPOP two CLLC modules, as depicted in Figure 2. The proposed ICB cells accomplish two main functions: (1) It can complete the resonance operation in the IPOP two CLLC modules; therefore, no extra inductors are required for resonance operation, (2) it can evenly distribute both the input and output currents among the IPOP two CLLC modules without complicated control schemes and dedicated controller. Compared to the existing IPOP current sharing techniques including control and magnetic based strategies, the proposed ICB cell has some distinct features such as: (1) it does not add additional hardware or magnetics to the IPOP system, (2) it can avoid auxiliary sampling and control circuits, thus, reduces the number of components and cost, (3) it has high reliability compared to complicated control schemes, (4) it is relatively easy to design, analyse, and implement.

3.1 | Magnetic structure of separate inductors and the proposed ICB cells using UU-cores

The resonant inductors of the IPOP two CLLC modules are designed with UU-cores structure as shown in Figure 4a, where two UU-cores are required for single inductor design. The magnetic structure of the proposed single ICB cell is shown in Figure 4b. The central UU-cores of the proposed ICB cell are coupled without airgap, which shows low reluctance to the magnetic flux lines and thereby provides strong coupling between two windings. Whereas, the outer UU-cores are attached to the central UU-cores with predetermined airgaps, which shows high reluctance to the magnetic flux lines and thereby provide sufficient resonant inductances for constituent CLLC modules [15, 19]. This structure of ICB cells can provide different leakage inductances on both sides for constituent CLLC modules. The direction of magnetic fluxes in Figures 4a–d are determined by the Right-Hand Rule.

3.2 | Magnetic structure of separate inductors and the proposed ICB cells using EE-cores

The magnetic structure of separate inductors and the proposed ICB cells using EE-cores are shown in Figure 4c,d. Figure 4c is added for explanation of Figure 4d. Here, the main focus was to design the proposed ICB cells using two EE-cores. Therefore, two EE-cores having airgap in the central limb are joined

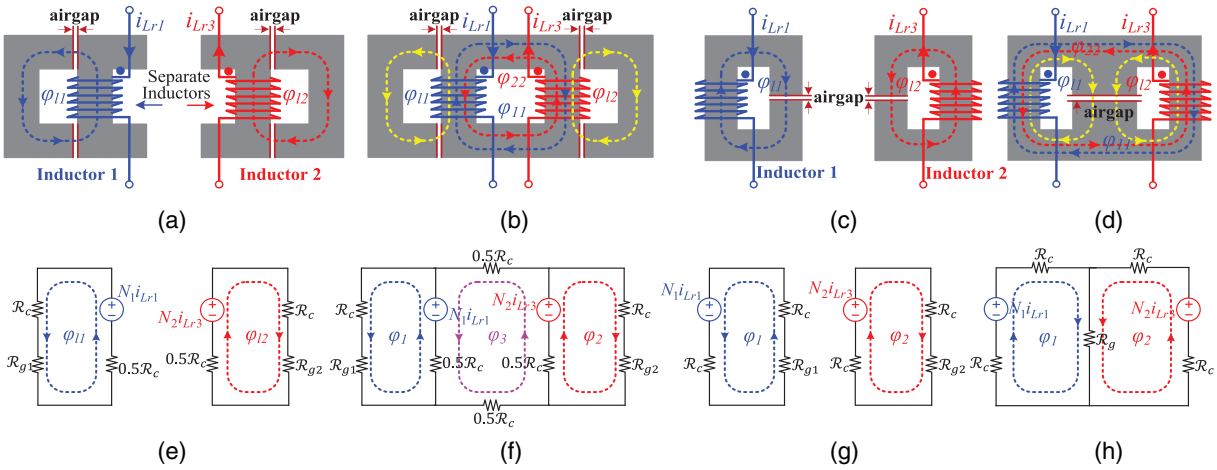

FIGURE 4 Magnetic structures of (a) separate inductors, and (b) proposed ICB cell with UU-cores. (c) Separate inductors, and (d) proposed ICB cell with EE-cores. Equivalent magnetic circuits (e), (f) separate inductors and ICB cell using UU-cores, and (g), (h) using EE-cores

together to shape the proposed ICB cells. The magnetic flux lines in the core have a low reluctance path in the outer limbs and thereby provides strong coupling between two windings. Whereas, the central limb shows high reluctance to the magnetic flux lines and thereby provide sufficient resonant inductances for constituent CLLC modules.

The ICB cell based on EE-cores require only two while the ICB cell based on UU-cores require four cores to shape the proposed cell. Thus, the number of cores can be reduced with EE-cores structure. The EE-cores cell structure is designed with an airgap in the central limb which cannot be changed once it is fixed. As a result, the resonant inductances on both sides are the same because of the same airgap sharing for both sides. Unlike UU-cores cells, the tolerances in resonant inductances cannot be realized in the experimental setup with EE-cores ICB cells. The blue and red colour flux lines in Figure 4b,d represent the main loops while the yellow colour flux lines represent the leakage fluxes in both ICB cells.

The design steps of separate resonant inductors shown in Figure 4a,c are provided in the Appendix Section.

3.3 | Electrical model of the proposed ICB cells

Based on the magnetic structure of the proposed ICB cells as shown in Figure 4b,d, a T-equivalent electrical model can be built as depicted in Figure 5. This model consists of 1:1 transformer, magnetizing inductance (L_m), and two leakage inductances (L_{lkp}, L_{lks}) on CLLC module 1 and 2 sides, respectively. The windings of the proposed ICB cells are inversely coupled. Therefore, the voltages v_1 and v_2 across the windings of inversely coupled coils can be expressed as follows:

$$\begin{cases} v_1 = L_{s1}\dfrac{di_{Lr1}}{dt} - M\dfrac{di_{Lr3}}{dt} \\ v_2 = L_{s2}\dfrac{di_{Lr3}}{dt} - M\dfrac{di_{Lr1}}{dt} \end{cases} \tag{1}$$

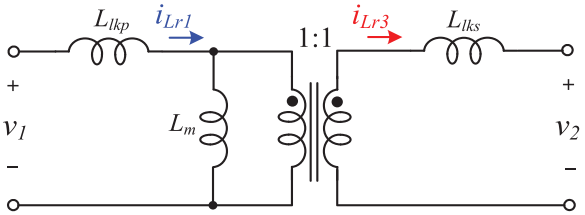

FIGURE 5 T-equivalent electrical model of the proposed ICB cells

where L_{s1} and L_{s2} are the self-inductances of the windings on left and right sides, and M is the mutual inductance between two coils. The mutual inductance of the proposed ICB cells can be obtained from the series L_{sr} and inverse series $L_{inv,sr}$ connection of the windings, and is given by:

$$\begin{cases} L_{sr} = L_{s1} + L_{s2} + 2M \\ L_{inv,sr} = L_{s1} + L_{s2} - 2M \end{cases} \tag{2}$$

Therefore, from (2) we obtained:

$$M = \left(L_{sr} - L_{inv,sr}\right)/4 \tag{3}$$

The self-inductances of the ICB cells can be measured at the primary/secondary side of the ICB cells while keeping open the secondary/primary side, respectively. Whereas, the leakage inductances and coupling coefficient of the ICB cells can be obtained as follows:

$$L_{lkp,s} = (1-k)\ L_{s1,s2},\ k = M/\sqrt{L_{s1}L_{s2}} \tag{4}$$

In case of $L_{s1} = L_{s2} = L_s$, the k and $L_{lkp/s}$ of the ICB cells can be obtained from $k = M/L_s$ and $L_{lkp} = L_{lks} = (1-k)\ L_s$.

3.4 | Current sharing performance of the proposed ICB cells

The current sharing performances of the proposed ICB cells are explained based on the electrical model and magnetic structures of the ICB cells in both steady-state and dynamic-state. The respective resonant tank currents generate magnetic fluxes in the cores shown in Figure 4b,d. These magnetic fluxes cancel out each other in the main loop because of the inverse coupling. In case of steady-state condition, the two currents are considered to be equal ($i_{Lr1} = i_{Lr3}$); thus, the magnetic fluxes generated by i_{Lr1} and i_{Lr3} will be equal in magnitude. As a result, the net magnetic flux will become zero in the main loop and thereby realizes even current sharing ($i_{Lr1} = i_{Lr3}$) in constituent modules. In case of dynamic-state condition, consider that initially $i_{Lr3} \geq i_{Lr1}$. Therefore, the magnetic flux generated by i_{Lr3} will be higher than the magnetic flux generated by i_{Lr1}. As a result, there exists some net magnetic flux in the main loop of the proposed ICB cells, which can be quantified using Ampere's circuital law and is given by:

$$\varphi_{net} = \frac{\mu_c \left(i_{Lr3} - i_{Lr1}\right) N_{icb} A_c}{l_m} \tag{5}$$

where μ_c, A_c, and l_m are the permeability, cross-sectional area, and magnetic path length of the core, while N_{icb} is the turns of the ICB cells.

The net magnetic flux in the core is responsible for current balancing in the constituent CLLC modules. This net magnetic flux will induce electromotive force, which in terms induces current. Therefore, according to Lenz's law it opposes its own cause producing it. Which results decrease in i_{Lr3} and increase in i_{Lr1}. Whenever, the difference of magnitude of the electromotive force on both sides of the ICB cells become equal to zero, the magnetic fluxes in the main loop will completely cancel out their effects and the net magnetic flux become zero in it. As a result, the two currents become equal in magnitude $i_{Lr3} = i_{Lr1}$ (it is valid for both cases ($i_{Lr3} \geq i_{Lr1}$ or $i_{Lr1} \geq i_{Lr3}$).

4 | ANALYSIS OF MAGNETIC CIRCUIT OF THE PROPOSED ICB CELLS

4.1 | Equivalent magnetic circuits of the proposed ICB cells using UU-cores

The equivalent magnetic circuits of separate resonant inductors and the proposed ICB cells using UU-cores are shown in Figure 4e,f. Figure 4e is added for the explanation of Figure 4f. The reluctances of the core $\mathcal{R}_c$ and airgaps $\mathcal{R}_g$ are considered in the equivalent magnetic circuits. In case of the proposed ICB cells using UU-cores as depicted in Figure 4f, the loop fluxes φ_1, φ_2 and φ_3 can be obtained from the loop equations. While the winding legs fluxes are the difference between the two fluxes for leg one and the sum of the two fluxes for leg two in the UU-cores. According to Faraday's law, the winding voltage depends on the derivate of fluxes of that limb where windings are wound, which can be expressed as follows:

$$v_1 = \frac{N_1 d\left(\varphi_1 - \varphi_3\right)}{dt}, \quad v_2 = \frac{N_2 d\left(\varphi_2 + \varphi_3\right)}{dt} \tag{6}$$

By putting the loop fluxes in (6), we can obtain voltages of the UU-cores ICB cells in terms of core and airgap reluctances, as documented from (A1), (A2) in the Appendix Section. By comparing (A1), (A2) with (1), we can obtain the self- and mutual inductance of the ICB cells. Which are reduced to (7) by assuming symmetrical structure of the ICB cells ($\mathcal{R}_{ag} = \mathcal{R}_{ag1} = \mathcal{R}_{ag2}$).

$$\begin{cases} L_{s1} = L_{s2} = \left(14\mathcal{R}_c^2 + 16\mathcal{R}_c\mathcal{R}_g + 4\mathcal{R}_g^2\right) N^2/\varkappa_2 \\ M = \left(4\mathcal{R}_c^2 + 8\mathcal{R}_c\mathcal{R}_g + 4\mathcal{R}_g^2\right) N^2/\varkappa_2 \end{cases} \tag{7}$$

where $\varkappa_1$ reduces to $\varkappa_2 = \mathcal{R}_c \left(15\mathcal{R}_c^2 + 22\mathcal{R}_c\mathcal{R}_{ag} + 8\mathcal{R}_{ag}^2\right)$. It is inferred from (7) that the same airgap results equivalent self-inductances. The leakage inductance of the proposed ICB cells is the difference between the self- and mutual inductance $L_{lkp/s} = L_{s1/s2} - M$. Therefore, from (7), the leakage inductance is given by:

$$L_{lkp/s} \cong N^2/\mathcal{R}_g\, \mathcal{R}_c \ll \mathcal{R}_{ag} \tag{8}$$

From (7), using the relation of $k = M/L_s$, we can obtain the equation of coupling coefficient with respect to the reluctances of UU-cores ICB cells reported in (A3). In case of UU-cores, k changes with change in airgap of the side UU-cores, which is formulated with extreme minimum and maximum limit of an airgap from (A3) in (9).

$$k = \begin{cases} \lim\limits_{\mathcal{R}_g \to 0} |k| = 0.28 \\ \lim\limits_{\mathcal{R}_g \to \infty} |k| = 1 \end{cases} \tag{9}$$

Theoretically, maximum k is equal to one; however, practically there always exist some leakage fluxes which limits the coupling coefficient to less than one. From (9), it is observed that the UU-cores structure of the ICB cells have minimum coupling coefficient when the side UU-cores are connected without airgap to the central UU-cores. In contrary, it is observed maximum with high airgap between the central and side UU-cores, which is depicted in Figure 6a.

4.2 | Equivalent magnetic circuits of the proposed ICB cells using EE-cores

In case of EE-cores, the equivalent magnetic circuits of separate inductors in Figure 4g are added for explanation of the proposed ICB cells magnetic circuit depicted in Figure 4h. Therefore, the proposed structure based on EE-cores with an airgap in the central limb is analysed here. From Figure 4h, the two loop fluxes of the EE-cores ICB cells can be derived from its loop equations. Using Faraday's law, the terminal voltages of

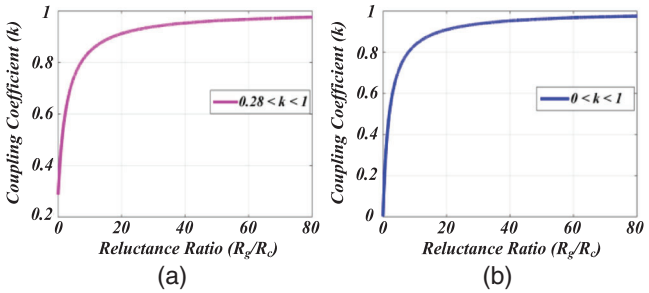

FIGURE 6 Plot of the coupling coefficient and reluctance ratio of the proposed ICB cells using (a) UU-cores structure, and (b) EE-cores structure

the ICB cells are obtained from (A4), (A5). By comparing (A4) and (A5) to (1), we can obtain the self- and mutual inductance of the EE-cores ICB cells, as follows:

$$\begin{cases} L_{s1} = L_{s2} = L_s = \left(\dfrac{2\mathcal{R}_c+\mathcal{R}_g}{4\mathcal{R}_c(\mathcal{R}_c+\mathcal{R}_g)}\right) N^2 \\ M = \left(\dfrac{\mathcal{R}_g}{4\mathcal{R}_c(\mathcal{R}_c+\mathcal{R}_g)}\right) N^2 \end{cases} \tag{10}$$

This exhibits same L_s on both sides of the cells. From (10), leakage inductance is the difference between L_s and M, and is given by:

$$L_{lkp} = L_{lks} \cong N^2/\mathcal{R}_g\,\mathcal{R}_c \ll \mathcal{R}_{ag} \tag{11}$$

The coupling coefficient of EE-cores is obtained from (10) in (12), which is formulated with extreme minimum and maximum limit of an airgap in (12); Likewise, in (9) for UU-cores.

$$k = \frac{M}{L_s} = \frac{\mathcal{R}_g}{2\mathcal{R}_c+\mathcal{R}_g},\; k = \begin{cases} \lim\limits_{\mathcal{R}_g\to 0} |k| = 0 \\ \lim\limits_{\mathcal{R}_g\to \infty} |k| = 1 \end{cases} \tag{12}$$

Theoretically, from (12) with no airgap in the central limb magnetically decouple the two windings. In adverse, maximizing the airgap in the central limb results high coupling between the two windings of the ICB cells, which is depicted in Figure 6b with the ratio of airgap and core reluctance. The k equals to one does not mean that the coupling of value one can be achieved practically. However, it can be increased by increasing both the self- and mutual inductance of the ICB cells.

5 | SIMULATION AND EXPERIMENTAL RESULTS

In this section, first, a hardware prototype of a single CLLC module was designed, fabricated, and tested with a 3.8-kW power rating. Which was then utilized as a reference module in the IPOP two CLLC modules. Besides, the CLLC module 2 was designed to validate the performance of both types of ICB cells in the IPOP two CLLC modules with a power rating of 4.9-kW.

TABLE 2 Circuit parameters of the IPOP two bidirectional CLLC modules

Parameters	Values/Part No.
Input voltage (V_{in})	400 V
Transformer turns ratio (n)	1:1
Switching frequency (f_{sw})	51 kHz
Power rating of single CLLC module	3.8-kW
Power rating of IPOP two CLLC modules	4.9-kW
MOSFETs	SPW47N60CFD
Transformer core	PQ5050
ICB cells cores	EE4220 and EE5555

TABLE 3 Parameters of the proposed ICB cell using UU-cores

Parameters	Values
Turns ratio of ICB cell	15:15
Self-inductance (L_{s1})	472.7 μH
Self-inductance (L_{s2})	475.1 μH
L_{sr}	1.797 mH
$L_{inv,sr}$	65.35 μH
Mutual inductance (M)	432.9 μH
Coupling coefficient (k)	0.913

TABLE 4 Parameters of the proposed ICB cell using EE-cores

Parameters	Values
Turns ratio of ICB cell	10:10
Self-inductance (L_{s1})	258.6 μH
Self-inductance (L_{s2})	259.1 μH
L_{sr}	961.4 μH
$L_{inv,sr}$	69.1 μH
Mutual inductance (M)	223 μH
Coupling coefficient (k)	0.861

The circuit parameters of CLLC modules are listed in Table 2. While Tables 3 and 4 enlist all parameters of the proposed ICB cells using UU- and EE-cores, respectively.

5.1 | Single bidirectional CLLC module

Figure 7 shows the experimental result of a single bidirectional CLLC module. It illustrates waveforms of the input voltage (V_{in}), square wave voltage input to the tank circuit (v_{ab1}), and resonant inductor currents of the primary and secondary sides (i_{Lr1}, i_{Lr2}), respectively. From equation of magnetizing inductor in (13), L_m is equal to 330 μH. This value is an optimal L_m value in case of efficiency point of view. However, higher L_m limits the gain curves of the CLLC converter. Therefore, theoretically

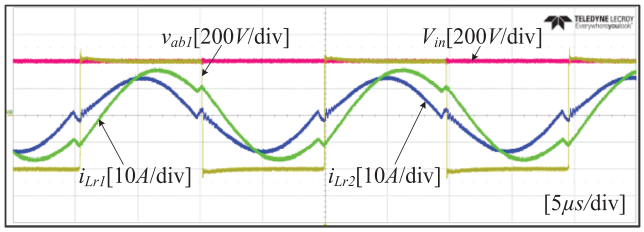

FIGURE 7 Experimental result of a single bidirectional CLLC module

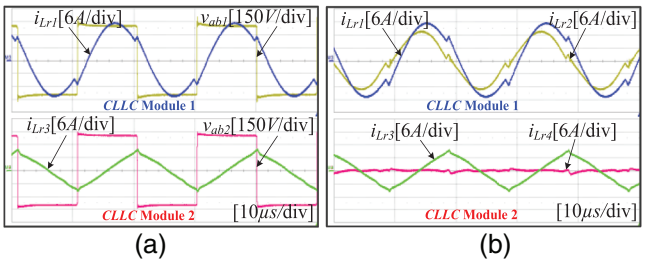

FIGURE 8 Experimental results in forward power flow direction with mismatched parameters and without proposed ICB cells. (a) Primary side MOSFETs bridge voltages (v_{ab1}, v_{ab2}) and resonant inductor currents (i_{Lr1}, i_{Lr3}) of constituent CLLC modules. (b) Resonant inductor currents at the primary (i_{Lr1}, i_{Lr3}) and secondary sides (i_{Lr2}, i_{Lr4}) of CLLC module 1 and 2, respectively

a lower L_m value of 170 μH is selected to obtain the gain curves monotonically decreasing and ensure ZVS operation in the whole operation range [24]. The L_m value is experimentally realized 167 μH by introducing airgap of 0.7 mm to the main transformer. Furthermore, a single bidirectional CLLC module is operated below the resonance point to ensure soft commutation of the secondary rectifier ($f_{sw} \leq f_r$):

$$L_m \leq \frac{t_{DT}}{16 C_{oss} f_{sw(max)}} = \frac{t_{DT}}{16 C_{oss} f_r} \tag{13}$$

where C_{oss} is the output capacitance of the switches, t_{DT} is the dead-time, and f_r, f_{sw} are the resonance and switching frequency of the converter.

5.2 | Proposed ICB cells based IPOP two CLLC modules in the forward power flow direction

The effectiveness of both types of proposed ICB cells are verified in the IPOP two CLLC modules with worst-case (case 1) in all of the cases listed in Table 1. The symmetric resonant tank circuit parameters for modules 2 based on reference module 1 were; $L_{m2} = 190$ μH, $L_{r3} = L_{r4} = 40.2$ μH, and $C_{r3} = C_{r4} = 247$ nF.

Figure 8 shows the experimental results of the IPOP two CLLC modules in the forward power flow direction with defined mismatches and without utilizing the proposed ICB cells. The power rating in this condition was 3.8-kW. It can

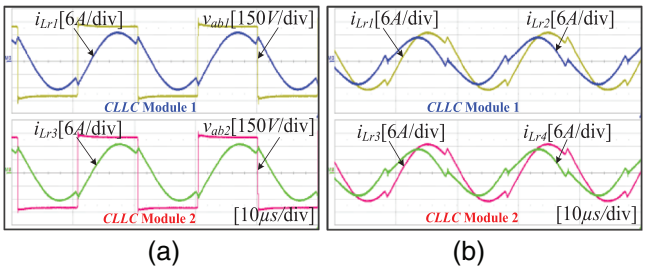

FIGURE 9 Experimental results in forward power flow direction with mismatched parameters and with proposed two ICB cells utilizing UU-cores. (a) Primary side MOSFETs bridge voltages (v_{ab1}, v_{ab2}) and resonant inductor currents (i_{Lr1}, i_{Lr3}) of constituent CLLC modules. (b) Resonant inductor currents at the primary (i_{Lr1}, i_{Lr3}) and secondary sides (i_{Lr2}, i_{Lr4}) of CLLC module 1 and 2, respectively

be seen from the waveforms in Figure 8a that the primary resonant inductor currents i_{Lr1} and i_{Lr3} of modules 1 and 2 are uneven. Similarly, the secondary side resonant inductor current i_{Lr4} of module 2 is almost zero, as shown in Figure 8b. Finally, it is inferred that the whole power is delivered by module 1, while module 2 does not take part in transferring power to the load. The i_{Lr3} of module 2 is similar to the magnetizing current. Thus, the waveforms exhibit the same condition predicted for the worst-case in simulation results discussed in Section 2. This uneven power distribution between CLLC modules in the IPOP configuration is a serious concern in high-power applications. Consequently, this can potentially damage the CLLC module with excessive power flow from it, when designed for low-power and exposed to handle high-power in the IPOP system. Therefore, this paper presents the promising solution for the uneven power flow in the IPOP two CLLC modules.

Figure 9 shows the experimental results with defined mismatches and with proposed ICB cells utilizing UU-cores. Figure 9a shows the even current sharing at the primary side between the IPOP two CLLC modules. This demonstrates the effectiveness of the proposed UU-cores ICB cells in the IPOP two CLLC modules. Moreover, Figure 9b interprets the experimental results with the ICB cells of the primary and secondary resonant inductors currents of the IPOP two CLLC modules. This can also clarify the even distribution of the secondary resonant inductor currents. Therefore, the proposed ICB cells based on UU-cores effectively overcome the uneven power distribution in the open-loop condition.

Furthermore, this paper also proposes ICB cells based on EE-cores. Simulation and experimental results are provided to verify the promising current sharing with the EE-cores ICB cells. As discussed, that the EE-cores provides equivalent inductances on both sides for resonance operation; therefore, mismatches in resonant inductances and practical imbalance shown in Figure 8 cannot be realized with EE-cores ICB cells. Accordingly, the imbalance in currents is realized through simulation results in PSIM, as shown in Figure 10. Figure 10a,b, verify that the mismatches in resonant capacitances ($C_{r3/4} = a \times C_{r1/2}$) and magnetizing inductance ($L_{m2} = b \times L_{m1}$) can still deteriorate performance of current sharing in the IPOP two CLLC modules with $L_{r3/4} = L_{r1/2}$ (where a and b are the 10 %

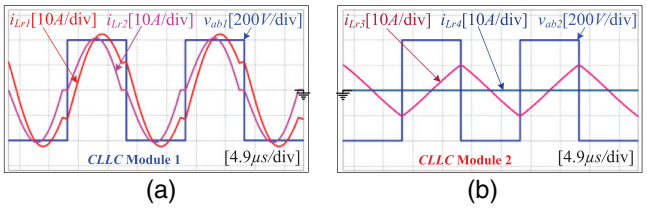

FIGURE 10 Simulation results without mismatches in the resonant inductances of the IPOP two CLLC modules. (a) CLLC module 1. (b) CLLC module 2

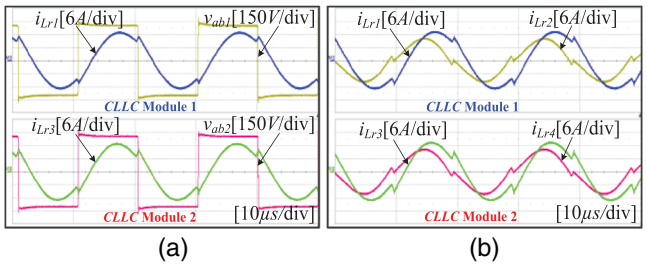

FIGURE 11 Experimental results in forward power flow direction with mismatched parameters and with proposed two ICB cells utilizing EE-cores. (a) Primary side MOSFETs bridge voltages (v_{ab1}, v_{ab2}) and resonant inductor currents (i_{Lr1}, i_{Lr3}) of constituent CLLC modules. (b) Resonant inductor currents at the primary (i_{Lr1}, i_{Lr3}) and secondary sides (i_{Lr2}, i_{Lr4}) of CLLC module 1 and 2, respectively

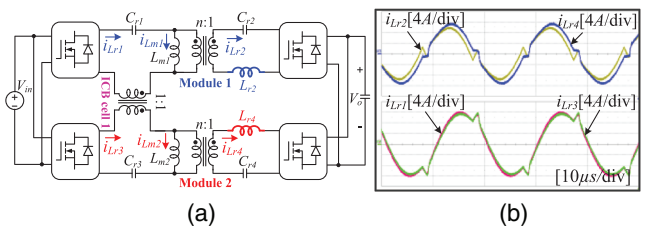

FIGURE 12 Proposed single ICB cell based IPOP two CLLC modules. (a) Circuit diagram, and (b) experimental result with single ICB cell

tolerances). The current sharing error and current distribution are similar to case 1 discussed in Section 2.

Figure 11a,b show the experimental results with defined mismatches and with proposed ICB cells utilizing EE-cores. Which validates the even current sharing between the IPOP two CLLC modules at the input as well as at the output of the converters. From Figures 9 and 11, it is inferred that the IPOP two CLLC modules based on the proposed both types of ICB cells inherent all of the good features of a single CLLC module including, ZVZCS.

5.3 | Single ICB Cell based IPOP two CLLC modules

The circuit diagram and experimental result of the IPOP two CLLC modules with single ICB cell are shown in Figures 12a and 12b, respectively. The difference in the secondary currents

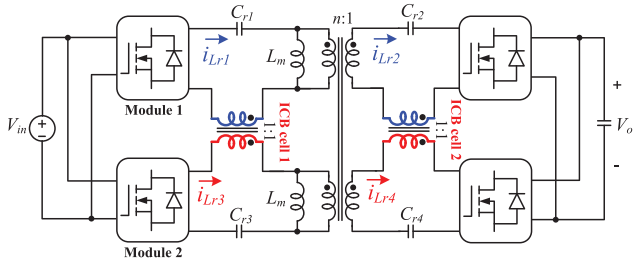

FIGURE 13 Proposed ICB cells based IPOP two CLLC modules with single magnetic link

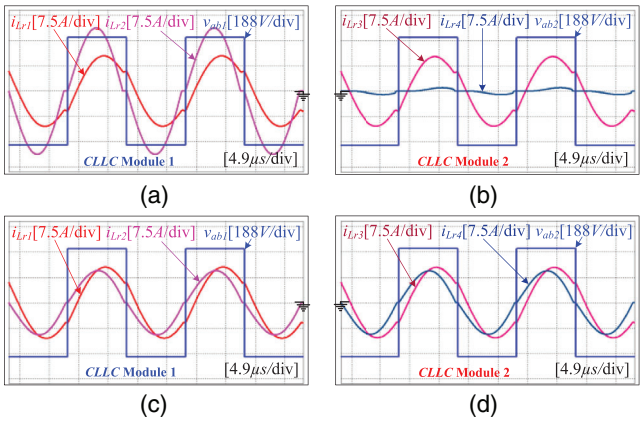

FIGURE 14 Simulation results of the IPOP two bidirectional CLLC modules with mismatched parameters using single magnetic link, (a)-(b) with ICB cell 1, and (c)-(d) with both proposed ICB cells. Where, v_{ab1}, v_{ab2} are the primary MOSFETs bridges voltages, and i_{Lr1}, i_{Lr3}, and i_{Lr2}, i_{Lr4} are the primary and secondary side resonant inductor currents of the IPOP two CLLC modules

is observed from the experimental result. It can be seen that i_{Lr2} is the difference between i_{Lr1} and i_{Lm1}, and i_{Lr4} is the difference between i_{Lr3} and i_{Lm2}. Therefore, the difference in i_{Lr2} and i_{Lr4} is caused by magnetizing currents of the main transformers because the primary side currents (i_{Lr1}, i_{Lr3}) are balanced by ICB cell 1. Practically, the tolerances in i_{Lm1} and i_{Lm2} are always exists in the main transformers, which results different secondary currents. This difference in the secondary currents can be quantified as follows:

$$\Delta\, i_{Lr} = \left| \frac{i_{Lm2} - i_{Lm1}}{i_{Lm1} + i_{Lm2}} \right| \times 100\% \tag{14}$$

Moreover, this difference in secondary currents causes different turn-off currents for rectifier of module 1 (i_{turn_off2}) and 2 (i_{turn_off4}), which are obtained as follows:

$$\begin{cases} i_{turn\_off2} = 0 \\ i_{turn\_off4} = n\,(i_{Lm1} - i_{Lm2}) \end{cases} \tag{15}$$

It is evident from (15) that module 2 loses ZCS feature at resonance with associated turn-off losses while using single ICB cell in the IPOP two CLLC modules. These effects of different rms and turn-off currents become even more severe in high output current applications. This current imbalance becomes

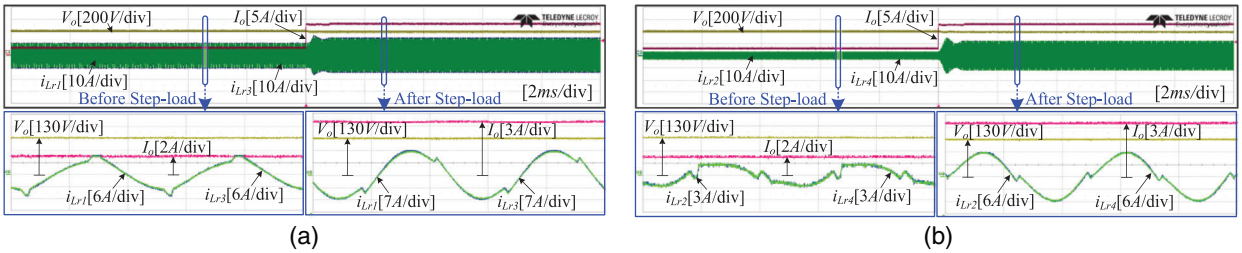

FIGURE 15 Step-load response of the IPOP two CLLC modules with proposed ICB cells when load resistance changes from 130 to 30 Ω. (a) Total load current (I_o), output voltage (V_o), and resonant inductor currents (i_{Lr1}, i_{Lr3}) at the primary sides of constituent CLLC modules with before and after step-load zoom-in waveforms, and (b) secondary sides currents (i_{Lr2}, i_{Lr4}) with before and after step-load zoom-in waveforms. (Zoom-in waveforms scale: 8 μs/div)

more severe in IPOP CLLC modules using single magnetic link compared to separate transformers, as depicted in Figure 13. The primary side imbalances are generated by the mismatches in primary circuit parameters while secondary side circuit mismatches are responsible for secondary currents imbalance. This is because of the single magnetic link in the IPOP two CLLC modules. Where, the sum of the primary currents is equal to the sum of the secondary currents ($i_{Lr1} + i_{Lr3} = i_{Lr2} + i_{Lr4}$); however, these currents are not necessarily be equal on primary side ($i_{Lr1} \neq i_{Lr3}$) as well as on the secondary side ($i_{Lr2} \neq i_{Lr4}$) due to mismatched circuit para- meters. It can be seen from the simulation results in Figure 14a,b, that the ICB cell 1 can evenly balance the primary currents ($i_{Lr1} = i_{Lr3}$); however, there is an imbalance in the secondary currents ($i_{Lr2} \neq i_{Lr4}$). Therefore, the ICB cell 1 cannot guarantee even power flow with single magnetic link. In this case, the need of ICB cell 2 become necessary to evenly share secondary currents ($i_{Lr2} = i_{Lr4}$). As discussed, that the proposed cells do not introduce additional magnetics; thus, utilizing the secondary resonant inductors can effectively solve this uneven power distribution. The simulation results in Figure 14c,d, show the effectiveness of the proposed ICB cell 1 and 2 in the IPOP two CLLC modules using single magnetic link. The experimental verification of Figure 14 is very similar to the one verified in Figures 9 and 11 using different ICB cells structures.

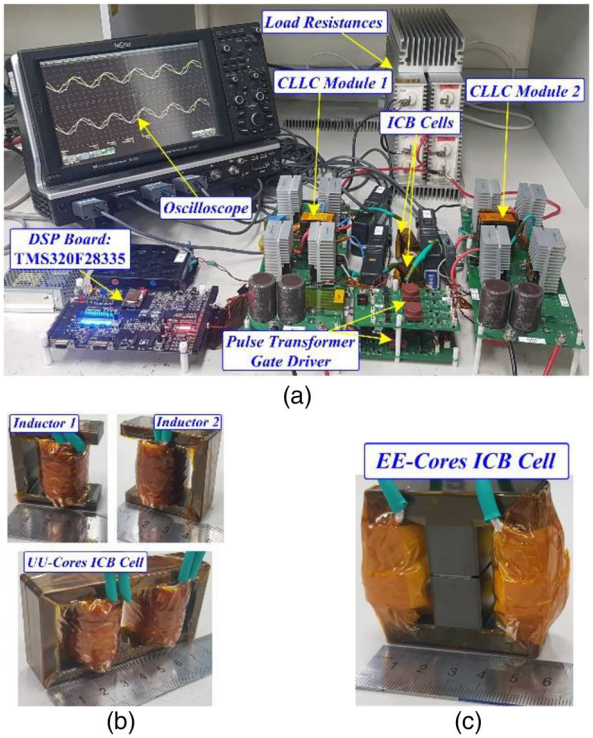

FIGURE 16 (a) Prototype picture of the IPOP two CLLC modules. (b) picture of the separate inductors and ICB cell using UU-cores, and (c) ICB cell using EE-cores

5.4 | Step-load response of the proposed ICB cells based IPOP two CLLC modules

A step-load response was made in the open-loop to verify the effectiveness of the proposed ICB cells in the transient state. In the step-load response, the load resistance was changed from 130 to 30 Ω in both waveforms with the output voltage of 380 V. Figure 15a shows the step-load response of the primary side currents of constituent CLLC modules with before and after the step-load zoom-in wave- forms. Besides, Figure 15b shows the step-load response of the secondary side currents of constituent CLLC modules with before and after the step-load zoom-in waveforms. Thus, the step-load experimental waveforms validate that the proposed ICB cells show good performance in current sharing during the transient state operation. Moreover, in Figures 15a,b, zoom-in waveforms before the step-load response verifies the current sharing performance at light-load condition (about 23% of the load).

The hardware prototype picture of the IPOP two CLLC modules is shown in Figure 16a; whereas, the picture of the separate inductors and the proposed ICB cell using UU- and EE-cores structure are shown in Figure 16b, c, respectively.

It is noteworthy to mention that the proposed ICB cells shows similar performances in the reverse power flow condition as well. Besides, the CS using proposed ICB cells is independent of the tank circuit gain or step up/down functions of the converter either in the forward or in reverse power flow conditions, as well as the asymmetric parameters design of the CLLC resonant tank circuit of the converter.

6 | CONCLUSION

Under the natural tolerances in the circuit parameters, the bidirectional CLLC modules have a serious issue of power imbalance in the IPOP configuration. To tackle this issue, a promising magnetic integration-based solution is proposed here. The already present inductors of the CLLC tank circuits are integrated to effectively overcome the power imbalance issue in the IPOP two CLLC modules. Two ICB cells are formed from four inductors to ensure both the input as well as the output current sharing with quantifiable tolerances in the circuit parameters. Besides, it does not increase the magnetic volume of the IPOP two CLLC modules. Apart from this, it ensures equal power distribution in the open-loop condition; therefore, it can avoid complex control algorithms for current sharing as well as reduce the component count and cost of the system. Two types of core structures are proposed and analysed in detail for the ICB cells. The UU-cores ICB cell require four cores while the EE-cores require two cores. Thus, it can also reduce the number of cores with EE-cores structure. The proposed ICB cells are as much effective in the backward power flow as it is in the forward power flow direction, which is experimentally verified in Section 5 with a 4.9-kW power rating. The commercial availability of both types of cores and the relatively simple design of the ICB cells make the proposed method more attractive to be adopted for industry practices.

ACKNOWLEDGMENT

This work was supported by the National Research Foundation of Korea (NRF) grant funded by the Ministry of Science and ICT (No. NRF-2022R1A2C2004874).

CONFLICT OF INTEREST

The authors declare that they have no known competing financial interests

DATA AVAILABILITY STATEMENT

Data available on request from the authors

ORCID

Ubaid Ahmad https://orcid.org/0000-0003-1788-7739

REFERENCES

1. Shi, J., et al.: Common-duty-ratio control of input-parallel output-parallel (IPOP) connected dc-dc converter modules with automatic sharing of currents. IEEE Trans. Power Electron. 27(7), 3277–3291 (2012)
2. Giri, R., Choudhary, V., Ayyanar, R., Mohan, N.: Common duty-ratio control of input-series connected modular dc-dc converter with active input voltage and load-current sharing. IEEE Trans. Power Electron. 42(4), 1101–1111 (2013)
3. Luo, S., Ye, Z., Lin, R.-L., Lee, F.C.: A classification and evaluation of paralleling methods for power supply modules. In: *Proceedings of the 30th Annual IEEE Power Electronics Specialists Conference. Record. (Cat. No.99CH36321)*, Charleston, SC, pp. 901–908 (1999)
4. Kim, J.W., Choi, H.S., Cho, B.H.: A novel droop method forconverter parallel operation. IEEE Trans. Power Electron. 17(1), 25–32 (2002)
5. Panov, Y., Rajagopalan, J., Lee, F.C.: Analysis and design of N parallel dc-dc converters with master-slave current control. Proc. IEEE APEC. 1, 436–442 (1997)
6. Yi, K.-H., Moon, G.-W.: Novel two-phase interleaved LLC series-resonant converter using a phase of the resonant capacitor. IEEE Trans. Ind. Electron. 56(5), 1815–1819 (2009)
7. Chen, H., *et. al.:* A current-sharing method for interleaved high-frequency LLC converter with partial energy processing. in IEEE Trans. on Ind. Electron. 67(2), 1498–1507 (2020)
8. Kim, H.-S., et al.: The high-efficiency isolated ac–dc converter using the three-phase interleaved LLC resonant converter employing the Y-connected rectifier. IEEE Trans. Power Electron. 29(8), 4017–4028 (2014)
9. Orietti, E., et al.: Two-phase interleaved LLC resonant converter with current-controlled inductor. In: Brazilian Power Electronics Conference COBEP, Bonito-Mato Grosso do Sul, Brazil, pp. 298–304 (2009)
10. Lin, B.R., Chen, P.L., Huang, C.L.: Analysis of LLC converter with series-parallel connection. In: *Proceedings of the 5th IEEE Conference on Industrial Electronics and Applications*, Taichung, pp. 346–351 (2010)
11. Lin, B., Dong, J.: ZVS resonant converter with parallel–series transformer connection. IEEE Trans. Ind. Electron. 58(7), 2972–2979 (2011)
12. Noah, M., et al.: A current sharing method utilizing single balancing transformer for a multiphase LLC resonant converter with integrated magnetics. IEEE J. Emerg. Sel. Topics Power Electron. 6(2), 977–992 (2018)
13. Liu, C., et al.: Magnetic-coupling current-balancing cells-based input-parallel output-parallel LLC resonant converter modules for high-frequency isolation of DC distribution systems. IEEE Trans. Power Electron. 31(10), 6968–6979 (2016)
14. Ahmad, U., et al.: Integrated current balancing transformer-based input-parallel output-parallel LLC resonant converter modules. In: *10th International Conf. on Power Electronics and ECCE Asia (ICPE 2019 ECCE-Asia)*, Busan, South Korea, pp. 1133–1140.
15. Ahmad, U., Cha, H., Naseem, N.: Integrated current balancing transformer-based input parallel output-parallel LLC resonant converter modules. IEEE Trans. Power Elec. 36(5), 5278–5289 (2021)
16. Liu, J., *et al.*: Current discrepancy mitigation of input-parallel output-parallel dual active bridge converters using coupled inductors. IEEE Trans. Ind. Electron. 68(9), 8182—8192. https://doi.org/10.1109/TIE.2020.3013793.
17. Kirshenboim, Peretz, M.M.: Combined multilevel and two-phase interleaved LLC converter with enhanced power processing characteristics and natural current sharing. IEEE Trans. Power Electron. 33(7), 5613–5620 (2018)
18. Tada, Y., Uno, M., Sato, Y.: Three-phase interleaved LLC asymm- etric resonant converter with capacitive current balancing and reduced switch voltage stress. IEEE Access. 8(1), 5688–5698 (2019)
19. Lee, J.-P., Cha, H., et al.: Analysis and design of coupled inductors for two-phase interleaved dc-dc converters. J. Power Electron. 13(3), 339–348 (2013)
20. Beiranvand, R., et al.: Using LLC resonant converter for designing wide-range voltage source. IEEE Trans. Ind. Electron. 58(5), 1746–1756 (2011)
21. Musavi, F., et al.: An LLC resonant dc-dc converter for wide output voltage range battery charging applications. IEEE Trans. Power Electron. 28(12), 5437–5445 (2013)
22. Hillers, A., Christen, D., Biela, J.: Design of a highly efficient bidirectional isolated LLC resonant converter. In *15th International Power Electronics and Motion Control Conference, ECCE Europe*, Serbia (2012)
23. Pledl, G., et al.: Theory of operation, design procedure and simulation of a bidirectional LLC resonant converter for vehicular applications. In: *Proceedings of the IEEE Vehicle Power Propulsion Conference*, Lille, France, pp. 1–5 (2010)
24. Jung, J.H., et al.: Design methodology of bidirectional CLLC resonant converter for high-frequency isolation of dc distribution systems. IEEE Trans. Power Electron. 28(4), 1741–1755 (2013)
25. Zahid, Z.U., et al.: Design of bidirectional dc-dc resonant converter for vehicle-to-grid (V2G) applications. IEEE Trans. Transp. Electrif. 1(3), 232–244 (2015)
26. Wm, C. McLyman, T.: Transformer and Inductor Design Handbook, 3rd Ed., Kg Magnetics, Inc., Idyllwild, CA (2004)

How to cite this article: Ahmad, U., Cha, H., Ro, J.-S.: Integrated current balancing cells based IPOP bidirectional CLLC resonant converter modules for high-power applications. IET Power Electron. 15, 1687–1698 (2022). https://doi.org/10.1049/pel2.12337

APPENDIX

Analysis of the UU-cores ICB cells

The voltages of the ICB cells with UU-cores are as follows:

$$v_1 = 2N^2\left(\frac{7\mathcal{R}_c^2 + 3\mathcal{R}_c\mathcal{R}_{g1} + 5\mathcal{R}_c\mathcal{R}_{g2} + 2\mathcal{R}_{g1}\mathcal{R}_{g2}}{x_1}\right)\frac{di_{Lr1}}{dt} - 4N^2\left(\frac{\mathcal{R}_c^2 + \mathcal{R}_c\mathcal{R}_{g1} + \mathcal{R}_c\mathcal{R}_{g2} + \mathcal{R}_{g1}\mathcal{R}_{g2}}{x_1}\right)\frac{di_{Lr3}}{dt} \tag{A1}$$

$$v_2 = -4N^2\left(\frac{\mathcal{R}_c^2 + \mathcal{R}_c\mathcal{R}_{g1} + \mathcal{R}_c\mathcal{R}_{g2} + \mathcal{R}_{g1}\mathcal{R}_{g2}}{x_1}\right)\frac{di_{Lr1}}{dt} + 2N^2\left(\frac{7\mathcal{R}_c^2 + 5\mathcal{R}_c\mathcal{R}_{g1} + 3\mathcal{R}_c\mathcal{R}_{g2} + 2\mathcal{R}_{g1}\mathcal{R}_{g2}}{x_1}\right)\frac{di_{Lr3}}{dt} \tag{A2}$$

where $x_1 = \mathcal{R}_c\,(15\mathcal{R}_c^2 + 11\mathcal{R}_c\mathcal{R}_{g1} + 11\mathcal{R}_c\mathcal{R}_{g2} + 8\mathcal{R}_{g1}\mathcal{R}_{g2})$.

The coupling coefficient of UU-cores can be written as:

$$k = \frac{4\mathcal{R}_c^2 + 8\mathcal{R}_c\mathcal{R}_g + 4\mathcal{R}_g^2}{14\mathcal{R}_c^2 + 16\mathcal{R}_c\mathcal{R}_g + 4\mathcal{R}_g^2} \tag{A3}$$

Analysis of the EE-cores ICB cells

Using Faraday's law, the terminal voltages can be obtained from (A4), (A5) while using the loop fluxes of the EE-cores.

$$v_1 = \left(\frac{N^2\left(2\mathcal{R}_c + \mathcal{R}_g\right)}{4\mathcal{R}_c\left(\mathcal{R}_c + \mathcal{R}_g\right)}\right)\frac{di_{Lr1}}{dt} - \left(\frac{N^2\mathcal{R}_g}{4\mathcal{R}_c\left(\mathcal{R}_c + \mathcal{R}_g\right)}\right)\frac{di_{Lr3}}{dt} \tag{A4}$$

$$v_2 = -\left(\frac{N^2\mathcal{R}_g}{4\mathcal{R}_c\left(\mathcal{R}_c + \mathcal{R}_g\right)}\right)\frac{di_{Lr1}}{dt} + \left(\frac{N^2\left(2\mathcal{R}_c + \mathcal{R}_g\right)}{4\mathcal{R}_c\left(\mathcal{R}_c + \mathcal{R}_g\right)}\right)\frac{di_{Lr3}}{dt} \tag{A5}$$

Resonant Inductor Design Steps

The design of the resonant inductor or AC inductor are quite similar to the design of transformer. Because there is no DC flux in the core both in resonant inductors as well as in transformer. Therefore, the apparent power (P) of an inductor that is the product of excitation voltage and current through the resonant inductor, which can be written as:

$$P = VA \tag{A6}$$

This volt-amp capability of a core is related to its area product (AP_{core}) [26], which can be written as follows:

$$AP_{core} = \frac{VA}{K_f K_u B_{ac} J f_{sw}} \tag{A7}$$

where K_f is the waveform factor ($K_f = 4.44$ for sine wave), K_u is the window utilization factor (this defines the maximum space occupied by the copper in the window), B_{ac} is the magnetic flux density in the core, J is current density, and f_{sw} is the operating frequency of the converter.

The AC inductor must support the applied voltage (V_{ac}); therefore, the number of turns (N) can be calculated using Faraday's law, as follows:

$$N = \frac{V_{ac}}{K_f A_c B_{ac} f_{sw}} \tag{A8}$$

where A_c is the cross-sectional area of the core. To achieve a desire inductance value of resonant inductor, an airgap (l_{ag}) from (A9) can be placed in the core.

$$l_{ag} = \frac{4\pi \times 10^{-7} N^2 A_c}{L_r} \tag{A9}$$

Based on the above design steps, the already present resonant inductors were designed and after that integrated to form the proposed ICB cells, as depicted in Figure 4b,d, of the paper. This makes the design of proposed ICB cells easy and intuitive.